PAPER

Check for updates

Study of proximity-coupled magnetic anisotropy in V-doped SnTe using spin resonance and magnetic measurements†

Subhadip Ghosh (ID) *[a] and Sanjeev Kumar Srivastava (ID) [b]

SnTe is a topological crystalline insulator with topological surface states (TSSs) protected by crystal symmetries. This, along with an associated Berry-phase π, results in a positive quantum correction in electrical conductivity, known as weak antilocalization (WAL). The applied magnetic field breaks down the TSS protection, resulting in a cusp-like negative magnetoconductance (MC). SnTe has a large amount (10^{21} cm^{-3}) of Sn vacancies, leading to considerable bulk conductivity with a parabolic background over the WAL MC. In this work, we observe an enhancement of the WAL signal in V-doped SnTe using electron spin resonance (ESR) measurements by substituting Sn vacancies with V atoms and charge-transfer-induced and temperature-dependent localization of itinerant carriers, called bound magnetic polarons (BMPs), which increases the effective mass of both electrons and holes and reduces bulk conductivity, as a consequence of magnetic anisotropy. Additionally, spin–orbit-coupling (SOC) induced spin canting, BMPs, interstitial, and substitutional occupation of V-impurities lead to competing ferromagnetic and antiferromagnetic proximity-coupled itinerant carrier-mediated Ruderman–Kittel–Kasuya–Yosida interaction in bare and V-doped SnTe, as evidenced by normal and parallel components of internal magnetic fields, observed in low-temperature ESR absorption spectral and temperature-dependent DC magnetization measurements. This proximity-coupled magnetic anisotropy makes V-doped SnTe a potential candidate for catalysis, thermoelectric, and spintronic applications. Density functional theory computations support SOC-induced spin canting, proximity-coupled magnetic order, and the charge transfer between V, Sn, and Sn vacancies.

1 Introduction

Topological materials have emerged as one of the most influential, interdisciplinary and rapidly expanding research fields of the last two decades, with the invention of numerous topological materials, including topological insulators (TI),[1] topological crystalline insulators (TCI),[2–4] Dirac semimetals,[5] Weyl semimetals,[6] topological superconductors[3] and others. TCIs have prospective applications in optoelectronics, spintronics,[3] quantum computing,[3,4] energy conversion,[7,8] catalysis[9] and quantum transport. The proximity-coupled order[10,11] of magnetic topological insulators[12–14] facilitates the room-temperature application of magnetic topological phases due to the interaction between the topological electronic states and the magnetic degrees of freedom.[10,15–17]

Topological crystalline insulators (TCIs) like SnTe, with a rock salt structure, exhibit four Dirac cones, with one on each of the (001) and(110) surfaces and two on the (111) surface centered at the Γ and M points,[2,18] while trivial topological insulators (TIs) such as Bi_2Te_3 and Bi_2Se_3[19,20] have only one Dirac cone. Angle-resolved photoemission spectroscopy (ARPES)[11,21–23] and scanning tunneling microscopy (STM)[24,25] confirm the presence of topological surface states (TSSs). Theoretical and experimental studies have shown that the formation energy of Sn vacancies is significantly lower than that of Te vacancies.[26–28] As a result, SnTe exhibits a high concentration of Sn vacancies (10^{21} cm^{-3}), which contributes to its semimetallic behavior. However, for SnTe, bulk conductivity, influenced by intrinsic p-type defects (10^{21} cm^{-3}),[2,3,29] contributes to negative magnetoconductance (NMC). Enhancing TSS conductance involves nanostructuring and doping strategies. Thin film growth techniques (MBE and CVD)[2,4,30] and chemical reduction methods (hydrothermal and solvothermal)[20,31] are widely used for the synthesis of nanostructured TCIs. Pb doping in SnTe reduces hole carrier density, while Fe,[19] Co,[20] Dy, Cu,[19] V,[14,32] Cr,[16,19,33] Eu,[18] and Mn[23,34,35] doping in TIs and TCIs enhances TSS conductance and induces magnetic ordering.

[a] School of Nano Science and Technology, Indian Institute of Technology, Kharagpur 721302, West Bengal, India. E-mail: subhadipjrc@gmail.com

[b] Department of Physics, Indian Institute of Technology, Kharagpur, West Bengal 721302, India. E-mail: sanjeev@phy.iitkgp.ac.in

This journal is © the Owner Societies 2025

Phys. Chem. Chem. Phys., 2025, **27**, 11499–11511 | 11499

Incorporating magnetic impurity in SnTe of the order of Sn vacancy concentration has reduced the contribution of hole conductivity by substitution or charge transfer-induced hole localization,[2,36–38] leading to topological quantum interference. Magnetic dopants introduce anisotropic interactions,[34,39,40] resulting in canted ferromagnetic (FM) and antiferromagnetic (AFM) states,[14,32] often explained by percolation theory[33,36–38,41,42] and RKKY interactions.[13,14,43] Electron spin resonance (ESR)[44–47] helps to distinguish bulk and surface characteristics, detecting signatures of magnetic interactions. At low temperatures, TCIs exhibit weak antilocalization (WAL) or weak localization (WL) effects,[47,48] which can be reversed by an external magnetic field,[47,48] affecting ESR spectra and revealing cyclotron resonance and SdH oscillations.[45,46]

In this paper, we have synthesized bare and V-doped ($0 < x < 0.08$) SnTe nanoparticles (NPs) using the chemical reflux method with a co-precipitation reaction mechanism. The present work is focused on studying the carrier-mediated magnetism, photoluminescence (PL), and weak antilocalization (WAL) effects in highly disordered SnTe and V-doped SnTe using SQUID, PL spectroscopy, and electron spin resonance (ESR) spectroscopy. To support ESR and SQUID results, other measurements such as X-ray diffraction (XRD), X-ray photoelectron spectroscopy, Raman scattering, and density functional theory (DFT) computation have been carried out.[2–4,45] Our computational investigation evaluates the role of Sn vacancies in the charge transfer, density of states (DOS), and band structure modulation of the simulated structures of SnTe and V-doped SnTe, including and excluding SOC.

2 Experimental section

2.1 Materials synthesis

$V_xSn_{1-x}Te$ ($x = 0$, 0.03, 0.05, and 0.08) nano-alloys are prepared by a simultaneous reaction using the chemical reflux method with a co-precipitation[49] reaction mechanism. $SnCl_2 \cdot 2H_2O$ (99.99%), $VCl_3 \cdot 6H_2O$, Te powder, glycine amino acid (as a surfactant reactant) and $NaBH_4$ (as a reducing agent) are used as precursors. At first, 1 mmol $SnCl_2 \cdot 2H_2O$ solution is prepared in a round bottom flask, and 5 mmol glycine is added. The solution is heated at 80 °C for 45 minutes with magnetic starring, and a grey-color colloidal Sn^{+2} solution is observed. At the same time, 1 mmol Te powder is taken in 20 mL of water, and 10 mmol $NaBH_4$ is added to the Te solution and left for 45 min with magnetic stirring to reduce Te into Te^{-2}.

$$2Te + 4NaBH_4 + 7H_2O \rightarrow 2NaHTe + Na_2B_4O_7 + 14H_2O \quad (1)$$

Then Te^{-2} colloidal solutions are mixed with the Sn^{+2} solution, and the condenser is connected to the mouth of the round bottom flask and left for 5 to 6 hours at 100 °C with magnetic starring. Finally, the obtained black precipitate is separated from the solution by centrifugation and cleaned with distilled water and 99.99% ethanol (several times) to remove unwanted impurities. After that, the black precipitate is dried in a vacuum hot air oven for 24 h to avoid unnecessary

oxidation in the presence of air. In addition to pristine SnTe, V-doped SnTe with different concentrations is prepared with VCl_3 as a source of V^{+2} ion. 0.03, 0.05, and 0.08 mmol $VCl_3 \cdot 6H_2O$ salt is added to 0.97, 0.95, 0.92 mmol $SnCl_2 \cdot 2H_2O$ solution for the preparation of 3%, 5% and 8% V doped SnTe. The same amounts of Te powder, glycine amino acid, and $NaBH_4$ are used as precursors. The resultant solution is processed *via* a similar procedure[49,50] and left for 6 hours at 100 °C with magnetic stirring. The obtained black precipitates are separated and collected using the above-mentioned procedure.

2.2 Characterization technique

The crystal structure and phase composition of the nano alloys are investigated by powder X-ray diffraction using a Bruker D2 phase 2nd generation X-ray diffractometer and Cu K_α = 1.5406 Å. The diffraction data are collected at room temperature with a step size of 4.67° per minute, over ($10° < \theta < 80°$). The morphology of the synthesized nanoalloys is explored using a Zeiss Supra 40 field-emission scanning electron microscope (accelerating voltage 200 kV) and JEM ARM 300 F2 high-resolution transmission electron microscope (accelerating voltage 300 kV) equipped with energy-dispersive X-ray spectroscopy (EDX) detectors. The ethanol pre-sonicated colloidal NP droplets are placed on a small thin glass wafer to perform field-emission-gun scanning electron microscopy (FEGSEM). Further stoichiometric verification is done by X-ray photoelectron spectroscopy using a PHI5000 Versa probe system equipped with an Al Kα ($h\nu$ = 1486.6 eV) source. The binding energies are charge referenced to C 1s at 284.6 eV. High-resolution XPS spectra are taken at 58.7 eV analyzer pass energy in a step size of 0.125 eV. XPS valence band spectra are taken at 23.5 eV analyzer pass energy in a step size of 0.125 eV. DC magnetization measurements are carried out using a quantum design MPMS SQUID VSM, attached with liquid He 3 cryostats. The symmetric vibration states of the nano-compounds are investigated by Raman spectroscopy using a T64000 (JY, France) micro-Raman spectrometer with an excitation wavelength of 532 nm. The complementary anti-symmetric vibrational states are investigated using the NICOLET 6700 FTIR spectrometer. The room temperature photo-luminance (PL) spectra are collected to investigate the modulation of charge transfer and band structure in the presence of defects and magnetic impurities. The room temperature and the low-temperature X band ESR spectra are recorded using a Bruker ELEXYS E-580 spectrometer for the investigation of magnetic interaction,[45–47] hyperfine Zeeman splitting[45,51] and topological quantum interference[46,52] of the observed compounds.

2.3 Computational details

We investigate the charge transfer effects, electronic structure, density of states, and magnetic properties of bare and impurity-doped topological insulators with Sn vacancies. All simulations are carried out using the plain wave DFT method implemented in the quantum espresso code.[53] The Purdue–Burke–Ernzerhof[54,55] scheme of the generalized gradient approximation (GGA) is used for the exchange–correlation potential.[54,55] The experimentally

11500 | *Phys. Chem. Chem. Phys.*, 2025, **27**, 11499–11511

This journal is © the Owner Societies 2025

reported lattice constant with $a = 6.32$ Å in FCC structure having the $Fm\bar{3}m$ space group is used as the initial parameter[29] and the CIF file is taken from the Materials Project Crystallographic database. We have taken a $2 \times 2 \times 2$ supercell structure of bare SnTe to further confirm the theoretical results. All cell atoms are relaxed using the Broyden–Fletcher–Goldfarb–Shannon (BFGS) quasi-Newton algorithm until the Hellmann–Feynman force reached 1 mRy per a.u. with the optimization energy of 10^{-9} Ry per a.u. A Sn atom has been removed from the SnTe unit cell and $2 \times 2 \times 2$ supercell to create Sn vacancies. All structures containing Sn vacancies were modeled with a total charge of +2 and adjusted using Makov–Payne electrostatic corrections to account for finite-size effects in charged supercells. Subsequently, we replaced one Sn atom with a V atom to investigate the magnetic proximity[3,11,17] in modulating the DOS, band structure, LDOS, and charge transfer effects of all of the above-simulated compounds. All structures containing a V atom but without Sn vacancies were also adjusted using Makov–Payne electrostatic corrections to account for electrostatic interactions in charged supercells. Optimization is performed for SOC and non-SOC calculations until inter-atomic force and stress become less than 10^{-5} eV Å^{-1}. We used the full relativistic pseudopotential for the noncollinear SOC calculation. The crystal structures are optimized with a kinetic-energy cut-off of 89 Ry and a charge-density cut-off of 810 Ry with $20 \times 20 \times 20$ K-mesh.

3 Results and discussion
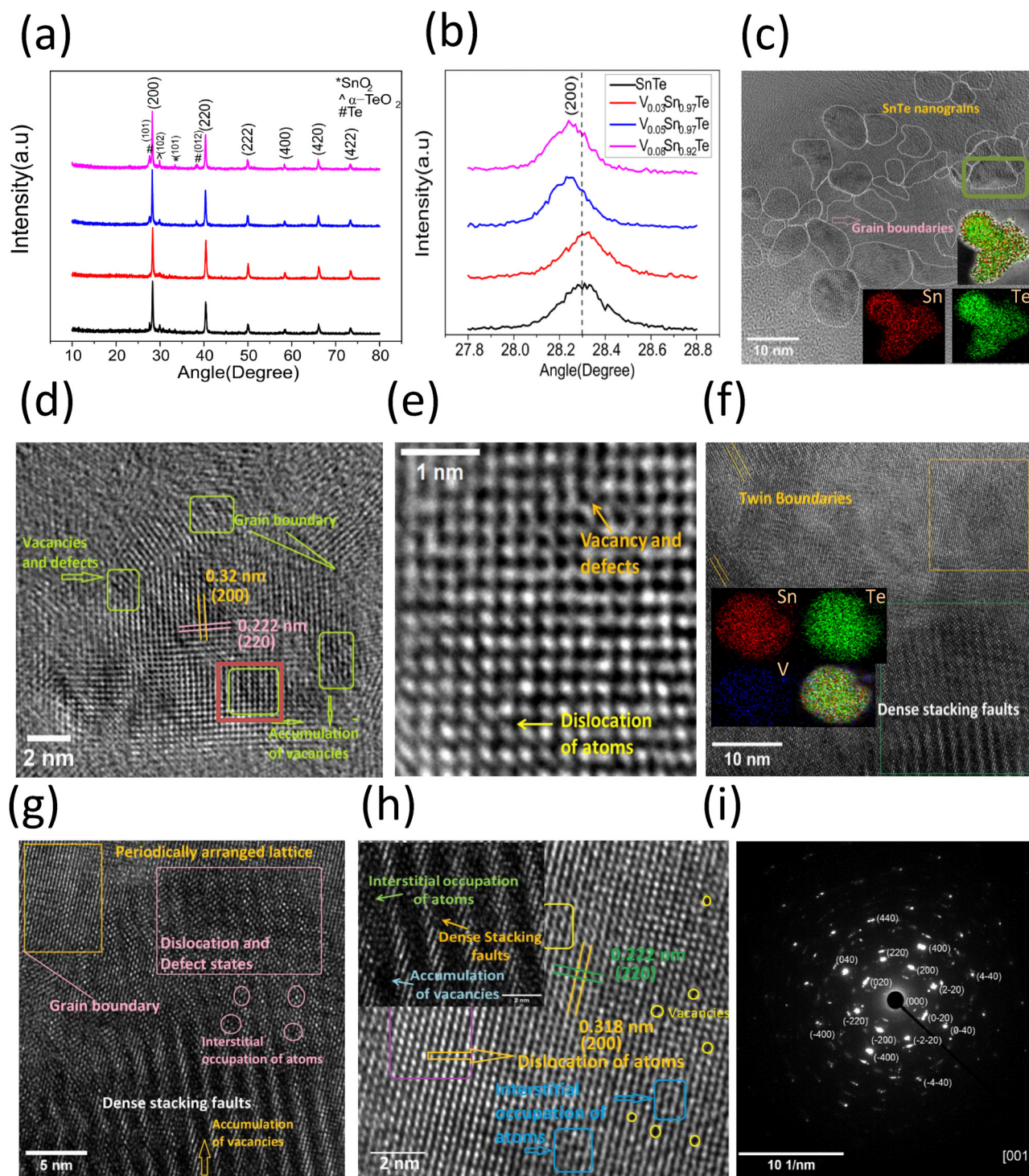
3.1 X-Ray diffraction

Fig. 1(a) shows the XRD patterns of the as-synthesized $V_x Sn_{1-x}Te$ samples. The prominent reflection peaks are observed at 2θ values of $28.30°$, $40.45°$, $50.10°$, $58.46°$, $66.20°$, and $73.40°$, aligning with the (200), (220), (222), (400), (420), and (422) planes of the FCC crystallographic structure of SnTe, characterized by octahedral symmetry, as confirmed through comparison with the joint committee on powder diffraction standard data.[8,29,56,57] Fig. 1(b) illustrates that the most intense (200) peak of $V_{0.03}Sn_{0.97}Te$ has shifted towards a higher diffraction angle, whereas $V_{0.05}Sn_{0.95}Te$ and $V_{0.08}Sn_{0.92}Te$ have shifted towards lower diffraction angles compared to bare SnTe. The radii of V^{+2} ions are less than those of Sn^{+2} ions. The observation indicates that at a lower doping concentration (3%), the substitutional occupation of vanadium is preferred, while at higher doping concentrations (5% and 8%), the interstitial occupation becomes more favorable. The observation of Te, TeO_2, and SnO_2 as impurity phases in bare SnTe, $V_{0.05}Sn_{0.95}Te$, and $V_{0.08}Sn_{0.92}Te$ indicates the presence of unreacted Te and surface oxidation of NPs. The minimal peak intensity of TeO_2 and SnO_2 compared to the SnTe characteristic (200) peak suggests a clear indication of surface oxidation of the NPs. Consequently, nearly phase-pure SnTe and $V_x Sn_{1-x}Te$ samples are produced without the segregation of the impurity phase.

3.1.1 FEGSEM and HRTEM. FEGSEM images of pristine SnTe and $V_x Sn_{1-x}Te$ ($x = 0.03, 0.05, 0.08$) V-doped compounds are shown sequentially in Fig. S1(c)–(f) (ESI†), respectively. The

morphology of NPs is characterized as a deformed circular disc,[30] exhibiting a diameter ranging from 20 to 50 nm. The insets of Fig. S1(c)–(f) (ESI†) and Table 1 present the FEGSEM EDX data and the estimated weight percentages of Sn, Te, and V for both the synthesized bare and V-doped SnTe samples. The clustering of the nanoparticles is probably a result of their magnetic properties and the weak van der Waals forces acting between them. The close agreement of the V percentage with the precursor concentration reveals the high quality of the sample.

The HRTEM images and SAED patterns of bare and 3% V-doped SnTe were recorded to examine nanoplates, defect states, and crystallinity. Fig. S1(a) and (b) (ESI†) display HRTEM images and EDX spectra, confirming a deformed circular disc-like morphology with radii of 5–50 nm. The formation of larger nanoparticles occurs as a result of coalescence-induced elongation driven by magnetic forces and van der Waals interactions. The weight percentages obtained from HRTEM EDX are consistent with the SEM EDX results, as shown in the insets of Fig. S1(a) and (b) (ESI†) and Table 1. Elemental mapping (Fig. 1(c) and (f)) reveals a consistent distribution of Sn, Te, and V, indicating the high quality of the sample.[7,56] Fig. 1(c) shows the bare SnTe nanograins and grain boundaries, where the smaller grains (5–10 nm) exhibit fewer defects and single crystallinity,[57,58] while the larger grains (10–50 nm) display more defects and polycrystalline structures.[59] The enlarged HRTEM image of a larger grain (Fig. 1(d)) reveals multiple defects. The interplanar spacings of the (200) and (220) planes in bare SnTe are 0.32 nm and 0.222 nm, consistent with the reported values.[7,56,57] The accumulated defects in approximately 10 nm grains suggest a lower crystallinity. The enlarged view of the red square marked region of Fig. 1(d), on a 1 nm scale, depicted the dislocation of the atoms, vacancies, and defects, shown in Fig. 1(e). The SAED pattern of bare SnTe (Fig. S1(c), ESI†) displays faint[7] and bright diffraction spots, which confirms its crystallinity. Certain diffraction spots (Fig. S1(c), ESI†) show deviations from the expected circular ring pattern, attributed to incomplete layers and defects.[59] Multiple orientations of planes further confirm polycrystallinity in larger grains. For $V_{0.03}Sn_{0.97}Te$, the enlarged HRTEM image (Fig. S1(b), ESI†) of a 47.32 nm grain shows twin boundaries,[58,59] dense stacking faults,[7,58] atomic dislocations,[58] and vacancies (Fig. 1(f)–(h)).[58] The (200) and (220) interplanar spacings of $V_{0.03}Sn_{0.97}Te$ are 0.318 and 0.222 nm, consistent with the literature.[7,56] The inset of Fig. 1(h) shows a clear visual of dense stacking faults, accumulation of vacancies, and interstitial occupation of atoms. The SAED pattern (Fig. 1(i)) displays a square diffraction spot arrangement, indicating improved crystallinity, consistent with fewer defect states in larger grains. The manifestation of the square SAED pattern in $V_{0.03}Sn_{0.97}Te$ reveals that the zone axis of the diffraction is [001].[57] The presence of split diffraction spots in the SAED pattern of $V_{0.03}Sn_{0.97}Te$ is the consequence of the increase or decrease of interplanar spacing due to the presence of internal and external stocking faults.[58,59] Consequently, HRTEM, SAED, elemental mapping, and EDX validate the crystallinity, defect states, and superior quality of the sample.

This journal is © the Owner Societies 2025

Phys. Chem. Chem. Phys., 2025, **27**, 11499–11511 | **11501**

Fig. 1 (a) XRD and (b) enlarged view of the (200) plane of SnTe and V_xSn_{1-x}Te (x = 0.03, 0.05, 0.08). (c) HRTEM image of SnTe nanograins; white encloser regions show SnTe nanograins and the corresponding grain boundaries (insets show the HRTEM EDX elemental mappings of Sn, Te, and SnTe, respectively, with 50 nm scale bar). (d) The enlarged view of the larger grain (enclosed by the green rectangle) shows the interplanar spacing of the (200) and (220) plains, grain boundaries, vacancies, defects, and accumulation of vacancies in different green rectangular enclosed regions. (e) The SAED pattern of bare SnTe. (f) HRTEM image of $V_{0.03}Sn_{0.97}$Te nanograins of 47.32 nm diameter shows twin boundaries, dense stacking faults, and various defect states (insets show the HRTEM EDX elemental mappings of Sn, Te, V, and $V_{0.03}Sn_{0.97}$Te, respectively, with 25 nm scale bar). (g) The enlarged view of the larger grain (enclosed by the yellow rectangle) shows the interplanar spacing of the (200) and (220) plains, vacancies, defects, dislocation, and interstitial occupation of atoms. (h) The enlarged view of the larger grain (enclosed by the green rectangle) shows dense stacking faults, accumulation of vacancies, interstitial occupation of atoms, grain boundary, dislocation, and defect states. (i) SAED pattern of $V_{0.03}Sn_{0.97}$Te.

11502 | *Phys. Chem. Chem. Phys.*, 2025, **27**, 11499–11511

This journal is © the Owner Societies 2025

Table 1 The atomic concentrations of Sn, Te, and V from EDX results

Sample name	Atomic% of Sn	Atomic% of Te	Atomic% of V
SnTe	52.12	47.88	0
SnTe$_{TEM}$	52.10	47.90	0
V$_{0.03}$Sn$_{0.97}$Te	56.33	42.23	1.444
V$_{0.03}$Sn$_{0.97}$Te$_{TEM}$	53.65	42.65	3.69
V$_{0.05}$Sn$_{0.95}$Te	57.01	38.14	4.85
V$_{0.08}$Sn$_{0.92}$Te	48.24	44.52	7.24

3.2 X-Ray photoelectron spectroscopy

XPS analysis was performed to confirm impurity phases and oxidation states, with all spectra charge-referenced to the C 1s peak at 285.6 eV.[20] Fig. 2(a)–(d) show high-resolution XPS spectra of the Sn 3d, Te 3d, V 3p, and O 1s regions, with survey spectra (Fig. S2(a), ESI†) validating the presence of Sn and Te. The Sn 3d$_{5/2}$ and Sn 3d$_{3/2}$ peaks of pristine SnTe at 485.85 eV and 494.3 eV[8,56,60,61] shift positively (0.05–0.15 eV) in V$_x$Sn$_{1-x}$Te (x = 0.03, 0.05, 0.08) due to charge transfer from Sn^{+2} ions to Sn vacancies. Surface degradation results in a Sn^0 state in V$_{0.03}$Sn$_{0.97}$Te, shifting negatively due to charge transfer from V.[60] Increased V doping creates additional Sn vacancies via interstitial V^{+4} occupation, further altering charge distribution. Surface oxidation produces Sn^{+4} peaks at 486.64 and 495 eV,[62] which shift slightly (0.06–0.4 eV) in V-doped samples. O 1s spectra at 530.2 eV and 529 eV for V$_{0.05}$Sn$_{0.95}$Te and V$_{0.08}$Sn$_{0.92}$Te confirm SnO$_x$[8,61,62] and TeO$_x$,[61,63] which reveal the surface oxidation of the mentioned compounds.[8,61] Peaks at 530.6 eV and 531.8 eV for all samples arise from hydroxyl (–OH) and carbonyl (C–O–C) groups due to ethanol adsorption during cleaning. Te 3d$_{5/2}$ and 3d$_{3/2}$ peaks in SnTe appear at 571.8 eV and 582.22 eV (Te^{-2}) and 576.13 eV and 586.59 eV (Te^{+4}).[8,60,61,64] In V$_x$Sn$_{1-x}$Te, Te^{-2} states shift by 0.2–0.25 eV due to charge transfer to Sn vacancies and V–Te bond formation, indicating a stronger V–Te bond than Sn–Te.[32] Te^{+4}

binding energy decreases at higher V doping due to partial oxidation (TeO$_x$) and increased Sn vacancies.[9] The intensity of the V 3p peak increases with V doping, which confirms the presence and increase of V with V doping. For V$_{0.03}$Sn$_{0.97}$Te, peaks at 39.11 eV, 40.55 eV, 43.69 eV, and 44.7 eV indicate substitutional (+2, +3) and interstitial (+4, +5) states. For V$_{0.05}$Sn$_{0.95}$Te and V$_{0.08}$Sn$_{0.92}$Te, V^{+2} and V^{+3} peaks shift positively (0.9 eV, 0.76 eV) due to charge transfer from V ions to Sn vacancies.[64] At x = 0.03, V primarily substitutes Sn in the +2 and +3 states, while at x = 0.05 and 0.08, the interstitial V^{+4} and V^{+5} dominate. XPS valence band spectra reveal Fermi level shifts with V doping, described in the ESI† section of this paper.

3.3 RAMAN and FTIR

Raman spectroscopy explores the symmetric vibrational modes of SnTe and V-doped SnTe NPs. In pure SnTe, octahedral symmetry (O$_h$) cancels the net dipole moment, deactivating the first-order Raman modes. Vacancies induce polarizability, activating frozen Raman modes, while doping disrupts FCC symmetry, restoring Raman activity.[29,57,65] SnTe exhibits A$_1$ and E$_{TO}$ phonon modes at 118.62 cm^{-1} and 138.10 cm^{-1} (Fig. S3(a), ESI†). In V-doped SnTe, both peaks shift towards the higher wave number side due to charge transfer from the V to SnTe matrix, increasing the force constant and bulk modulus.[8,65] At higher doping concentrations, the shift remains constant as V occupies both substitutional and interstitial sites, causing opposing vibrational shifts.[29,65] Again, the lighter V atoms reduce the V–Te bond mass and shift Raman peaks towards higher wave numbers $\left(\omega = \sqrt{k/\mu}\right)$. The lower intensity in V$_{0.03}$Sn$_{0.97}$Te suggests reduced Sn vacancies due to V^{+2} substitution.[57,65] The presence of the A$_1$ and E$_{TO}$ modes in all samples confirms the high quality of the sample.

FTIR spectroscopy[50] complements Raman spectroscopy by detecting asymmetric molecular vibrations. Fig. S3(b) (ESI†) shows the FTIR spectra of bare and V-doped SnTe, where doping reduces peak intensity and shifts peaks to higher wavenumbers due to stress in NPs and charge transfer,[66] respectively. The peaks observed at 492.89 cm^{-1} and 636.85 cm^{-1} are associated with the vibrations of Te–Sn–Te and Sn–Te–Sn,[50] respectively. The Te–Sn–Te vibration appears first, attributed to its lower reduced mass. A new peak at 796.82 cm^{-1} is observed, resulting from Te–V–Te vibrations. The presence of common H–O stretching, H–O–H bending, and C–O, C–O–H stretching shows that the surface of NPs is associated with dangling H$_2$O, –COOH, and CO$_2$ molecules.[50,66] These results confirm charge-transfer effects, phase formation, and surface carboxyl (–O–C–O) and hydroxyl (–OH) groups, supporting the observed XPS O 1s spectra.

The presence of Urbach's tail in UV-VIS-NIR spectra is attributed to defects found in bare, doped, and surface-modified nanoparticles, leading to inaccuracies in the estimation of the band gap due to interband states.[67] FTIR transmittance, facilitated by a Michelson interferometer and Fourier transform, is more effective in identifying sub-bandgap states and actual band gaps.[67] Bulk SnTe exhibits a band gap of 0.18 eV,[60,61] and the UV-vis-NIR spectra (performed but not presented) span from 1.23 to
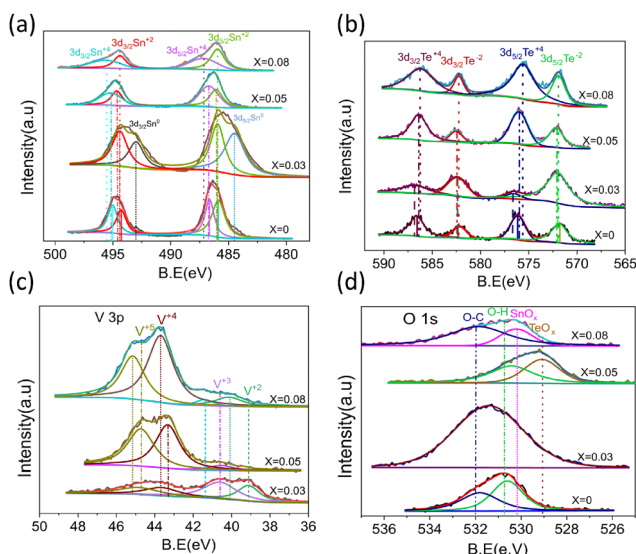
Fig. 2 HRXPS spectra of SnTe and V doped SnTe for (a) Sn 3d$_{5/2}$ and 3d$_{3/2}$ states and their deconvolution. (b) Te 3d$_{5/2}$ and 3d$_{3/2}$ states and their deconvolution. (c) V 3p$_{3/2}$ and 3p$_{1/2}$ states and their deconvolution, and (d) O 1s state and its deconvolution.

This journal is © the Owner Societies 2025

Phys. Chem. Chem. Phys., 2025, **27**, 11499–11511 | **11503**

4.13 eV, resulting in broadband absorption with Urbach's tail.[50,66] FTIR, with a range of 0.045–0.495 eV, is better suited for narrow-band semiconductors. Fig. S3(c) (ESI†) presents the Tauc plot of SnTe and $V_x Sn_{1-x}Te$ (x = 0.03, 0.05, 0.08), showing band gaps of 0.31 eV, 0.3 eV, 0.372 eV, and 0.41 eV, respectively. The widening of the band gap results from nanostructuring and the presence of cationic defect states. The sample with 3% V doping exhibits the lowest band gap, attributed to the presence of minimal vacancies and the role of V as a donor impurity. Increased doping levels (x = 0.05, 0.08) lead to a widening of the band gap due to the introduction of additional Sn vacancies by interstitial V^{+4} ions. These findings are consistent with XPS and DFT computations.

3.4 Photoluminescence spectroscopy

Symmetric ideal SnTe does not exhibit PL spectra; however, the presence of intrinsic Sn vacancies and defect states leads to observable PL emission. Photoluminescence spectroscopy elucidates these defects and impurity states. The PL spectra (Fig. S3(d), ESI†) of bare SnTe at 769.40 nm, 786.82 nm, 868.39 nm, and 955.01 nm are attributed to intraband transitions associated with defects, anti-sites, and cationic/anionic vacancies,[11,68] as corroborated by DFT simulations. The incorporation of V modifies defect states, resulting in the emergence of new PL peaks.[50,66] The 769.40 nm peak disappears with V doping, while a new 852.83 nm peak emerges due to V impurity states. Peaks at 786.82 nm, 955.94 nm, and 926.32 nm show a redshift, indicating denser defect states with V doping. In contrast, the 870.21 nm peak exhibits blue shifts. The red and blue shifts of the PL peaks after the incorporation of the V impurity corroborate the modulation of the band structure of V-doped SnTe. PL quenching in $V_{0.03}Sn_{0.97}Te$ corresponds to reduced Sn vacancies due to V^{+2} substitution, which is consistent with the minimum Raman intensity of this composition. The enhanced PL intensity in $V_{0.05}Sn_{0.95}Te$ and $V_{0.08}Sn_{0.92}Te$ indicates elevated defect concentrations due to interstitial V atoms, which is also reflected in the elevated Raman intensity of these compositions.

3.5 DFT computations

DFT computations reveal charge transfer-induced hole localization and magnetism in bulk and V-doped SnTe with an FCC structure ($Fm\bar{3}m$ space group). The role of Sn vacancies with V doping was analyzed using the PBE exchange–correlation scheme in Quantum Espresso.[54,55] Charge transfer and magnetic proximity effects were established via V substitution or interstitial incorporation with Sn vacancies. Theoretical and experimental studies have shown that SnTe has a high concentration of Sn vacancies due to lower formation energy of Sn vacancies than that of Te vacancies.[26–28] Fig. S4(a)–(f) and S10(a)–(f) (ESI†) illustrate the FCC structure with the $Fm\bar{3}m$ space group of SnTe, SnTe with Sn vacancies (Sn_VTe), V-doped SnTe (VSnTe), V-doped SnTe with Sn vacancies (VSn_VTe), SnTe with interstitial V (vSnTe), and SnTe with Sn vacancies and interstitial V (vSn_vTe), in the unit-cell and 2 × 2 × 2 supercell, respectively. Sn vacancy and V impurity formation energy in the 2 × 2 × 2 supercell is 3.46 eV and 2.56 eV, respectively. The obtained formation energy values are consistent with the literature.[26–28] Fig. S5(a)–(f) and
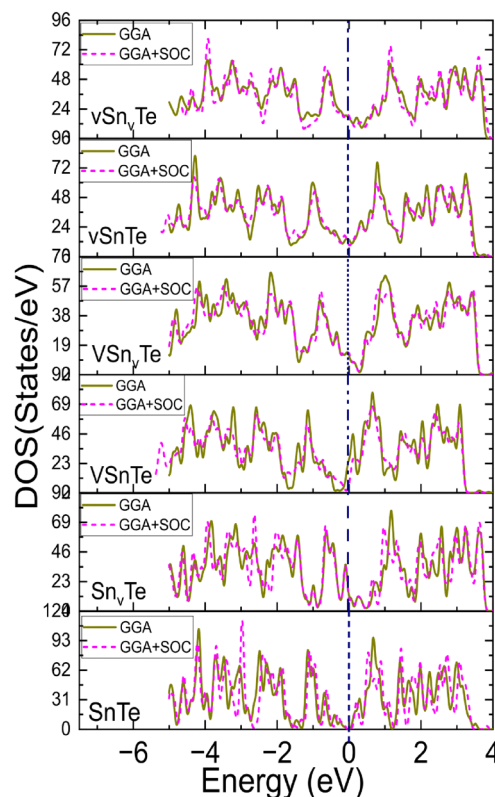

Fig. 3 DOS with GGA and GGA+SOC of SnTe, Sn_VTe, VSnTe, VSn_VTe, vSnTe, and vSn_vTe in the 2 × 2 × 2 supercell structure.

S6(a)–(f) (ESI†) depict DOS and band structures using GGA and GGA+SOC of six simulated unit cell structures mentioned above. Fig. 3 shows the DOS of six simulated 2 × 2 × 2 supercell structures mentioned above. Non-collinear GGA+SOC calculations reveal SOC-induced magnetic anisotropy[34,35,39,40] from spin flipping. The computed band gaps for SnTe are 0.06 eV (GGA) and 0.228 eV (GGA+SOC),[1,29] which are consistent with the experimental value of 0.31 eV. The DOS of Sn_VTe indicates a shift of the Fermi level towards the valence band, confirming the Sn vacancies as acceptors in p-type SnTe. Non-collinear GGA+SOC calculations yield a magnetic moment of 0.01 and $0.05\mu_B$ per cell in the unit cell and supercell structures, respectively, attributed to SOC-induced spin flipping near Sn vacancies. Both VSnTe and vSnTe defects shift the Fermi level toward the conduction band, exhibiting magnetic moments of 3.01 and $1.29\mu_B$ per cell in the unit cell and 3.47 and $1.64\mu_B$ per cell in the supercell, respectively; when V substitutes Sn^{+2} as V^{+2}, its localized 3d orbital contains three unpaired electrons, leading to a magnetic moment close to $3\mu_B$ per cell. The size of the octahedral hole in SnTe is 93 pm, and V can occupy an interstitial site in the V^{+4} state, with an ionic radius of 86 pm. In this oxidation state, the V atom has one unpaired 3d electron, contributing a magnetic moment close to $1\mu_B$ per cell. These considerations suggest that V can substitute Sn^{+2} as V^{+2} ions or occupy an interstitial site as V^{+4}, acting as a donor impurity. For VSn_VTe and vSn_vTe the magnetic moments are reduced to 2.17 and $1.06\mu_B$ per cell for the unit cell and 3.05 and $1.19\mu_B$ per cell for the supercell.

11504 | *Phys. Chem. Chem. Phys.*, 2025, **27**, 11499–11511

This journal is © the Owner Societies 2025

This reduction in the moment is attributed to charge transfer from V to Sn vacancies, which introduces localized states.[37,69] The observed decrease in magnetic moment implies the presence of antiferromagnetic interactions among localized charge.[20,36,37,70]

According to Z. Ma *et al.*, the work function of bulk SnTe[61,71] is 4.68 eV, while that of vanadium[72] is 4.3 eV. Nanostructuring increases[71,72] the work function of both SnTe and vanadium, revealing strong charge transfer from V to Sn atoms. To quantify charge transfer efficiency, we compare unpolarized Lowdin charge densities of (100) planes for SnTe, Sn_VTe, VSnTe, and VSn_VTe, depicted in Fig. S8(a)–(d) for the unit cell and S11(a)–(f) (ESI†) for the $2 \times 2 \times 2$ supercell, respectively. The increase in contour radii in the 2D charge density plot indicates charge transfer to the Sn vacancy. Fig. S9(a) and S12(a) (ESI†) compare the local density of states (LDOS) of the Sn 3d orbitals in the unit cell and supercell, respectively. The average localized integrated valence band charge of the Sn atom in SnTe is 0.0078 a.u. (0.00558 a.u. for the unit cell), reducing to 0.00417 (0.00428 a.u. for the unit cell) in Sn_VTe, confirming 0.00363 a.u. (0.00141 a.u. for the unit cell) charge transfer to the Sn vacancy. The charge content of the Sn 3d orbitals increases in VSnTe and VSn_VTe due to the charge transfer from V, shown in Table SI for the unit cell and SIII (ESI†) for the supercell, respectively. The interstitial V of vSnTe and vSn_VTe enables van der Waals bonding, easing the additional charge transfer to SnTe,[32] as shown in Table SI for the unit cell and SIII (ESI†) for the supercell, respectively. The reduced localized charge of V in V-doped SnTe with Sn vacancies further supports this charge transfer (Tables SII and SIV, Fig. S6(b), ESI†). Incorporating SOC with noncollinear interactions induces hybridization[3,17] with higher atomic orbitals, resulting in proximity coupling[10] in the Sn 4d and V 5d orbitals.

3.6 Magnetization

Magnetically, SnTe is diamagnetic, while V is paramagnetic. The field-cooled (FC) and zero-field-cooled (ZFC) *M–T* curves at 500 Oe for SnTe (Fig. 4(a)) show bifurcation near room temperature. Non-collinear DFT computations indicate that the SOC-induced magnetic moment cancels out in the ideal SnTe, making it diamagnetic. However, Sn vacancies introduce small ferromagnetic interactions due to SOC-induced spin flipping, forming BMPs.[29,68] An appreciable amount of charge transfer from the SnTe matrix to the Sn vacancy position is confirmed by the charge density contour plots and valence band charge of the Sn 3d and V 4d orbitals. XPS confirms charge transfer from Sn to Sn vacancies in $V_xSn_{1-x}Te$ (x = 0.03, 0.05, 0.08). This carrier-mediated semi-localization increases the electron and hole effective mass,[36–38] generating semi-magnetic order or localized moments. The vacancy in the SnTe matrix produces magnetocrystalline anisotropy,[68] indicating appreciable thermomagnetic irreversibility in the ZFC–FC curves of bare and V-doped compounds.[39,40,73] The ZFC curve of bare SnTe drops slowly and sharply beyond 289.6 K and 60 K, indicating competing FM and AFM[23,74] interaction due to the freezing of spins (spin-glass) and RKKY type itinerant carrier-mediated double exchange interaction among BMPs,[10,37,38,68,73] respectively.
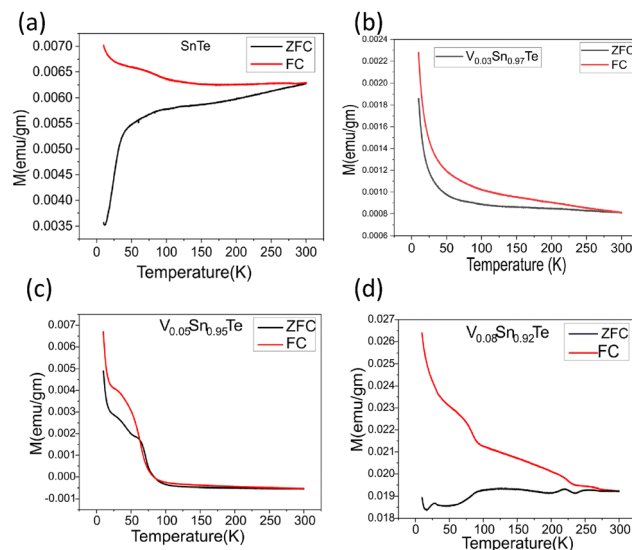

Fig. 4 *M–T* ZFC and FC curves at 500 Oe from 10 K–300 K for (a) SnTe, (b) $V_{0.03}Sn_{0.97}Te$, (c) $V_{0.05}Sn_{0.95}$, and (d) $V_{0.08}Sn_{0.92}$.

The *M–H* curve of SnTe (Fig. 5(a)) has a negative slope, confirming diamagnetism, with an upward shift suggesting weak ferromagnetism. SOC is the key determining factor for a material to be topological. V^{+2} or V^{+4} ions in substitutional or interstitial positions[13] experience crystal field splitting,[73] leading to hybridization and s–d/p–d exchange.[32,43] This induces spin canting and magnetic proximity effects.[10,11,39,40] In the dilute magnetic regime, the individual induced moments of the impurity-ligand dimer interact through the itinerant carrier-mediated RKKY double exchange interaction.[10,13,43,73]

$V_{0.03}Sn_{0.97}Te$ exhibits reduced hole concentration due to the Sn vacancies replaced by V.[32] DFT calculations give magnetic moments of 3.01 and 1.29μ_B per cell, indicating V^{+2}
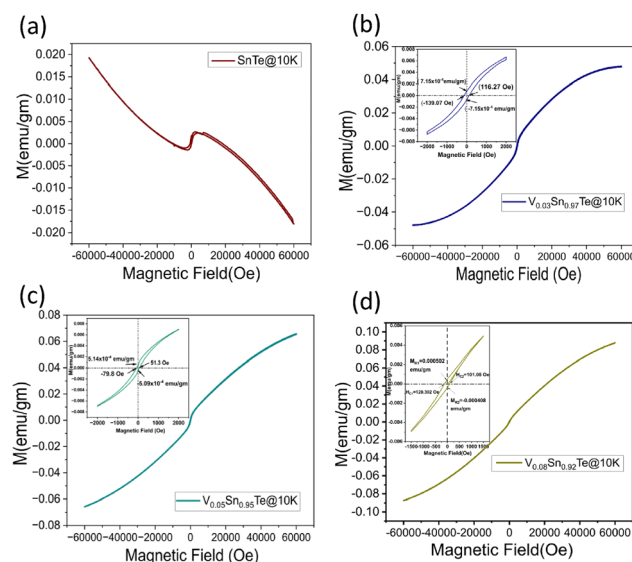

Fig. 5 *M–H* curves of (a) bare SnTe, (b) $V_{0.03}Sn_{0.97}Te$, (c) $V_{0.05}Sn_{0.95}Te$, and (d) $V_{0.08}Sn_{0.92}Te$ at 10 K.

This journal is © the Owner Societies 2025

Phys. Chem. Chem. Phys., 2025, **27**, 11499–11511 | **11505**

substitution and V^{+4} interstitial occupation, as described in the DFT results. The FC–ZFC M–T@500 Oe (Fig. 4(b)) curve bifurcates at 267.08 K and beyond 267.08 K (T_{irr}), a gradual upturn in the FC and ZFC curve indicates competing FM–AFM interactions.[74] FM arises from RKKY interactions among BMP and V–Te proximity-coupled induced magnetic moments for substitutional doping of V^{+2} ions and V–Te-induced moments,[3,10,13,17,43,73] while interstitial V^{+4} ions induce Sn vacancies, breaking crystal symmetry and opening the band gap.[43] This introduces an Ising term, leading to BR-type AFM RKKY interactions,[43] which is shown in the schematic S6 (ESI†). The M–H curve (Fig. 5(b) and its inset) shows hysteresis with remanent magnetization (7.15 × 10^{-4} emu per g), coercivity (127.67 Oe), and saturation magnetization (0.04815 emu per g), confirming FM dominance. For $V_{0.05}Sn_{0.95}Te$ (Fig. 4(c)), FC–ZFC curves show a broad blocking temperature range, indicating anisotropic FM–AFM competition.[74] This is probably due to the possible BR-correlated AFM interaction[13] overcome or comparable to the above-mentioned FM interaction due to the minimal substitutional V^{+2} or V^{+3} ions, confirmed by the XPS result. Below 70.65 K and 24 K, upturns in FC–ZFC curves reflect localization of the itinerant carrier with decreasing temperature, which increases the corresponding Fermi wavelength (λ_F) and makes the RKKY interaction ferromagnetic.[13] M–H (Fig. 5(c)) curves indicate superparamagnetic/paramagnetic surface components, with coercivity (65.55 Oe) and retentivity (5.14 × 10^{-4} emu per g) at the lowest observable temperature (10 K), shown in the inset of Fig. 5(c). Removing paramagnetic contributions reveals a saturation magnetization of 0.06574 emu per g. The nonsaturating superparamagnetic/paramagnetic surface components[44] of the M–H curve at the higher magnetic field regime originate from non-interacting or weakly interacting spins within BMPs and surface anisotropy.[3,44] The M–T and M–H curves of $V_{0.08}Sn_{0.92}Te$ are depicted in Fig. 4(d) and 5(d), respectively. The continuous increasing and decreasing trend of the ZFC curve is the signature of competing FM–AFM interactions[74] due to the comparable substitutional and interstitial occupation of the V impurity and the itinerant carrier-dependent oscillating RKKY interaction with temperature.[13,43] The broad ZFC and FC curves reveal a wide distribution of the blocking temperature (T_B), approximately close to 277 K. The FC and ZFC curves bifurcate at 276.2 K. The sudden upturn of the FC curve and the increasing separation between the FC and ZFC curves at 230.2 K and 81.07 K are the consequences of magnetic anisotropy[34,35,39,40] along the magnetic hard and easy axes, respectively. Subtracting the paramagnetic contribution from the M–H curve reveals a saturation magnetization of 0.0958 emu per g, with a coercivity of 110.676 Oe and a retentivity of 0.000455 emu per g. The sudden sharp increase in ZFC and FC curves below 20 K for all V-doped compounds is a consequence of surface-state-assisted enhancement of magnetic order[10] at the interface because, at this temperature, the chiral carriers of the surface of TCI are activated.[10] The above results conclude that intrinsic Sn vacancies and substitutional and interstitial occupation of the V^{+2} and V^{+4} ions lead to a competing FM and AFM correlation,[74] as temperature-dependent localization of the itinerant carrier results in an oscillating RKKY interaction.[10,13,36,37,43,73]

3.7 Electron spin resonance

To investigate the anisotropic anomalous behavior of chiral and impurity electrons under SOC, defects, and impurities, electron spin resonance (ESR) has been studied.[34,35] ESR spectroscopy[12,15,46–48,75] probes exchange interactions in transition metals and paramagnetic systems. In weakly coupled magnetic systems, single-crystal spectra result from the superposition of non-equivalent spins, while strong exchange interactions lead to exchange narrowing and collapsed spectra.[46–48,75] Hyperfine interactions provide additional anisotropy[34,35,39,40] insight. Besides the tuned magnetic field of the TE_{102} cavity, unpaired electrons are sensitive to their local environment.[45–48] Fig. 6(a) and (b) show room-temperature and low-temperature (14 K) ESR spectra of bare SnTe and V-doped SnTe. Bare SnTe exhibits a dip-like signal (inset of Fig. 6(b)) at g = 2.052, likely due to trapped electrons at Sn vacancies.[76,77] V has a nuclear moment I = 7/2 and hyperfine Zeeman splitting[51,74,78] into eight components[76,77] appears in both low- and room-temperature spectra. Even at low impurity concentrations (x = 0.03), splitting is observed at room temperature, with intensity reduced nearly sevenfold from low temperature. The Landé g factor at the microwave absorption peak reveals normal and parallel internal magnetic field components, leading to sixteen ESR absorption components,[77,78] confirming magnetic anisotropy in nanocompounds.[39,40,75,76] Fig. 6(c) shows the variation of normal and parallel Landé g factors with the nuclear magnetic quantum number (m_I), reinforcing magnetic anisotropy.[34,35,39,40,44,75,76] The slope of the parallel component is 2.5 times larger than the normal component, while the normal component's intensity is 1.76 times higher, indicating an easy axis along the normal direction and a hard axis along the parallel direction, consistent with non-collinear DFT results.[44,75] The Landé g factor for both components decreases with increased doping concentration, suggesting weaker electron interactions at 3% V doping due to reduced vacancies and increased separation between V impurities. Higher doping increases Sn vacancies and enhances itinerant carrier-mediated RKKY interaction[45,75] and the g value. The $g_\perp$ values of $V_xSn_{1-x}Te$ (x = 0.03, 0.05, 0.08) are 2.0217, 2.0237, and 2.02482, indicating stronger V interactions at higher doping levels. Fig. 6(d) shows the variation of the hyperfine splitting parameter (A)[34,35,51,74] with m_I. The $A_\perp$ component remains nearly constant, while $A_\parallel$ exhibits a slight decaying trend, illustrating nanocompound anisotropy.[34,35,40,51,74] The inset of Fig. 6(d) displays the variation of the large axial zero-field splitting parameter (D) (Kramers doublets)[45–47] with V concentration. At 14 K, D values for $V_xSn_{1-x}Te$ (x = 0.03, 0.05, 0.08) are 8.5967, 9.728, and 10.236 GHz × h, respectively. Increased V doping enhances defect concentration and RKKY interaction, strengthening the axial field[75] and increasing D. The D parameter depends on anion covalency, with Te > Se > S due to decreasing electronegativity.[45] This results in Te exhibiting a larger D parameter. Some studies attribute D increment to anisotropic Korringa relaxation[34,35,40,74] via Bloch–Wangsness–Redfield theory,[34,35,51] which is linked to strong spin–orbit coupling in heavy elements.[74]

11506 | *Phys. Chem. Chem. Phys.*, 2025, **27**, 11499–11511

This journal is © the Owner Societies 2025

The ESR spectral intensity is proportional to the first derivative of the microwave-cavity quality factor (Q) to the magnetic field (dQ/dB), as revealed by magnetic field modulation within the lock-in-detection approach.[48,53] The cavity Q factor determines
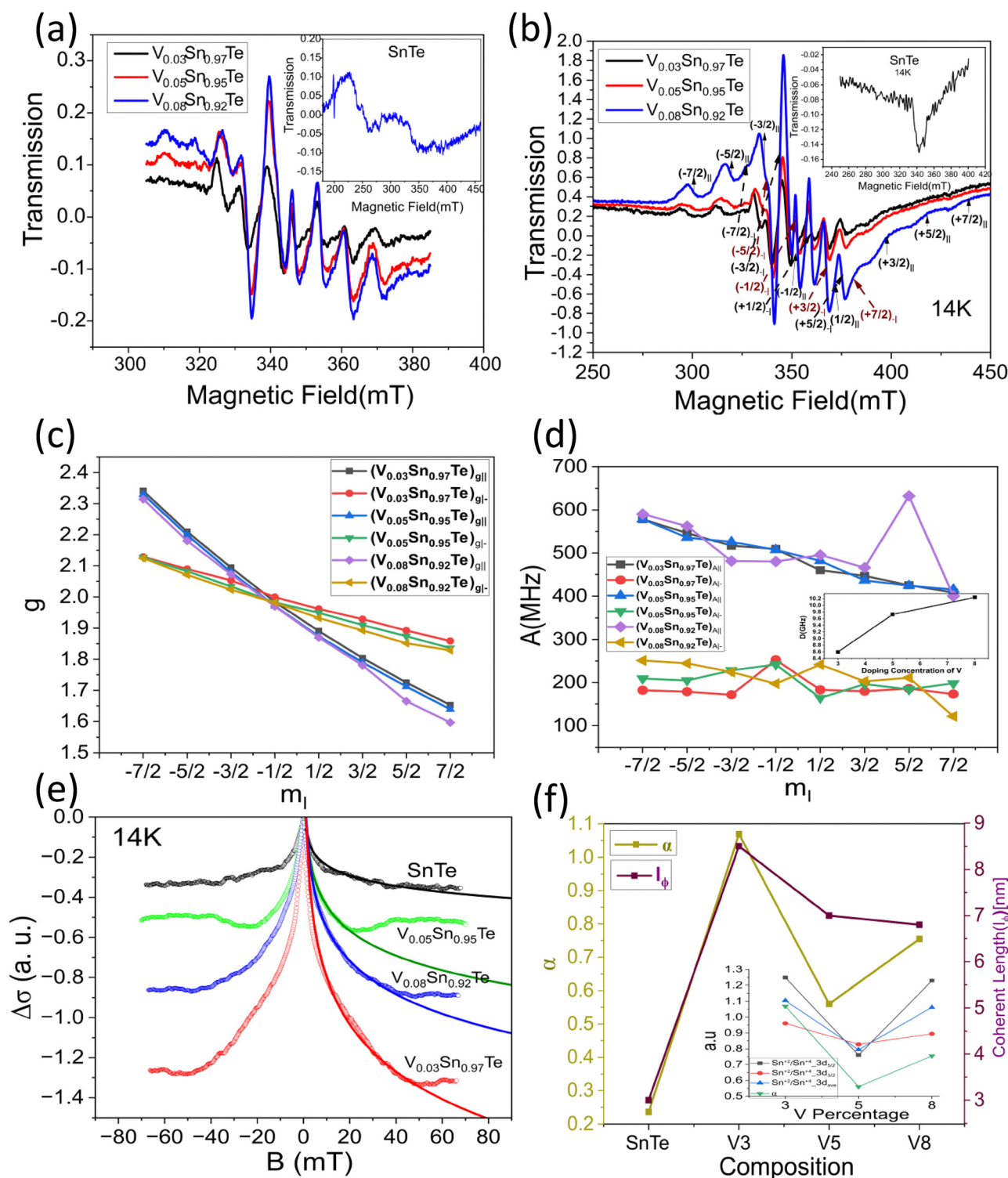
Fig. 6 (a) Comparison of room-temperature ESR spectra of V-doped compounds, (b) comparison of low-temperature (14 K) ESR spectra of V-doped compounds, the inset shows the ESR spectra of bare SnTe. (c) Comparison of normal and parallel components of the Landé g factor of bare and 3%, 5%, and 8% V doped compounds, and (d) the variation of the hyperfine splitting parameter (A) with the total nuclear magnetic quantum number (m_I). The inset shows the variation of the large axial zero-field splitting parameter (D) with doping concentration. (e) Comparison of low temperature (14 K) ESR integrated conductivity of SnTe, $V_{0.03}Sn_{0.97}$, $V_{0.05}Sn_{0.95}$, and $V_{0.08}Sn_{0.92}$, and their fitting with the HLN equation, and (f) the variation of coherence length (l_ϕ) and α with V-doping concentration. The inset shows the variation of the Sn^{+2}/Sn^{+4} (Sn^0 for V3) ratio and α with V doping concentration.

This journal is © the Owner Societies 2025

Phys. Chem. Chem. Phys., 2025, **27**, 11499–11511 | **11507**

sample conductivity and energy absorption in a tuned magnetic field, making the ESR signal strength linearly related to conductivity variations. Unlike contact measurements such as PPMS, ESR provides highly accurate differential conductivity.[46–48,53] ESR spectroscopy measures WL and WAL[15,48,52,79] with high accuracy, independent of impurity phases like SnO_2 and TeO_2.[48] Electrons following diffusive random walks exhibit magnetoconductance in topological insulators.[48] Spin-momentum locking minimizes backscattering, reducing resistance and increasing conductivity, leading to WAL effects.[46,47] A magnetic field disrupts the Berry phase, decreasing conductivity and enhancing backscattering, causing weak localization (WL). The applied magnetic field reverses the phase of scattering electrons,[48] generating positive (WL) or negative (WAL) magnetoconductance.[79] X-band (9.7 GHz) CW-ESR at 14 K in the zero-field regime provides differential magnetoconductivity of the TCI system. Fig. S2(b) (ESI†) and Fig. 6(e) compare the differential and integrated magnetoconducting behavior of SnTe and $V_xSn_{1-x}Te$ (x = 0.03, 0.05, 0.08). $V_{0.03}Sn_{0.97}Te$ exhibits maximum intensity due to minimal defect-induced anisotropy via Sn vacancy occupation by V^{+2} ions and prominent reduction of surface degradation, which is shown in the inset of Fig. 6(f). The negative magnetoconductivity of $V_{0.05}Sn_{0.95}Te$ is smaller than $V_{0.08}Sn_{0.92}Te$, as V^{+4} interstitial occupation creates additional Sn vacancies, which enhance surface degradation and increase bulk conductivity. This indicates that hole localization or reduction via Sn vacancy substitution enhances topological conductivity of chiral electrons mediated through an even number of Dirac cones of topological crystalline insulators (SnTe).[2–4,7,30] The cusp-like negative magnetoconductivity variation is due to the WAL effect in topological surface states (TSSs). Fitting the MC curve with the HLN (Hikami–Larkin–Nagaoka) equation[2,20] will further confirm WAL effects.

$$\Delta G(H) = \frac{\alpha e^2}{\pi h}\left[\Psi\left(\frac{\hbar}{4eHl_\varphi^2} + \frac{1}{2}\right) - \log\left(\frac{\hbar}{4eHl_\varphi^2}\right)\right] \quad (2)$$

where Ψ is the digamma function, l_ϕ is the coherence length, and $\Delta G(H)$ is the conductance, which is proportional to the conductivity σ of the sample, and α is a prefactor determining the fraction or number of independent transport channels involved in topological conductance from topological surface states (TSSs).[20] The best possible HLN fits are shown in Fig. 6(e). The Sn vacancy activates the surface degradation of SnTe NPs.[80,81] Doping with V reduced surface degradation.[18] The Sn^{+2}/Sn^{+4} ratio of the HRXPS spectra characterized the surface degradation of SnTe and V-doped SnTe. The variation of the Sn^{+2}/Sn^{+4} ratio with V doping concentration for $3d_{5/2}$ and $3d_{3/2}$ orbitals, along with their average, is directly proportional to the variation in α, as illustrated in the inset of Fig. 6(f). These results confirm that TSS response arises from the undegraded portion of V-doped SnTe. The fit for SnTe in the low-magnetic field range is satisfactory due to the low-temperature localization of itinerant carriers and the formation of a bound magnetic polaron (BMP) via Coulomb interactions. Crystal symmetry is the key determining factor for TSS states of TCI materials, such as SnTe. Discrepancies at higher temperatures (14 K) and magnetic fields arise from the delocalization of carriers and the migration of vacancies, which reduces the crystal

symmetry. That's why at higher temperatures and fields, the topological surface state (TSS) conductivity (WAL effects) and coherence length (l_ϕ) are suppressed by bulk carrier transport.[2,4] The fit for $V_{0.03}Sn_{0.97}Te$ is consistent across all field ranges, showing enhanced negative magneto-conductivity due to Sn vacancy substitution and prominent reduction of surface degradation. $V_{0.05}Sn_{0.95}Te$ fits well at low fields but diverges at high fields due to interstitial V^{+4} ions producing an additional Sn vacancy, which reduces crystal symmetry due to migration of vacancies. Again, additional Sn vacancy enhanced surface degradation, which is reflected in XPS spectroscopy. The Sn^{+2}/Sn^{+4} ratio observed in the HRXPS spectra of $V_{0.05}Sn_{0.95}Te$ reveals a minimum value compared to other compositions, indicating a clear signature of enhanced surface degradation. This degradation leads to a reduction in TSS states and consequently affects α, as illustrated in the inset of Fig. 6(f). Again, the reduction of TSS states emerges as an axion insulator or a quantum anomalous spin hall state,[10] which gives anomalous magnetoconductance, reflected in all compositions at high temperature and magnetic field range. Still, for $V_{0.05}Sn_{0.95}Te$, it arises at a relatively lower magnetic field due to surface degradation and a relatively higher concentration of vacancies due to interstitial occupation of V^{+4} ions. $V_{0.08}Sn_{0.92}Te$ fits well across entire ranges due to Sn vacancy substitution and prominent reduction of surface degradation. The HLN curve for SnTe and V-doped compounds (x = 0.03, 0.05, 0.08) was fitted to integrated ESR magnetoconductivity to extract parameters such as the prefactor (α) and coherence length (l_ϕ), ensuring realistic values (Fig. 6(e)). V-doped compounds exhibit improved α and l_ϕ due to reduced surface degradation, Sn vacancy substitution, and charge transfer-induced hole localization within NPs. Table 2 and Fig. 6(f) show the extracted values, which are consistent with previous reports.[2–4,30]

Theoretically, one transport channel is fitted with one Dirac cone for typical topological insulators like Bi_2Te_3, Bi_2Se_3, etc., with α = 0.5. The top and bottom surface states influence two surface transport channels with α = 1. SnTe has four Dirac cones on its topological surface. The presence of both the upper and lower surfaces gives eight transport channels with α = 4.[2,30] The value of α at 14 K of SnTe is 0.2358 $\mp$ 0.08, which is reasonable and shows that the contribution of the TSS transport channel is small due to surface degradation and intrinsic hole conductivity. The increase in α values for $V_xSn_{1-x}Te$ (x = 0.03, 0.05, 0.08) V-doped compounds reveals the reduction in surface degradation, hole conductivity by substituting Sn vacancies and charge transfer-induced localization of itinerant carriers, which enhances the conductivity of TSSs. This anisotropic behavior of magnetoresistance is evidence of magnetic anisotropy within the NPs.

Table 2 Coherence length (l_ϕ) and prefactor determining the fraction or number of independent transport channels (α) for typical data measured at 14 K presented in Fig. 6(e)

Sample name	l_ϕ (nm)	α
SnTe	3 $\pm$ 2	0.2358 $\mp$ 0.08
$V_{0.03}Sn_{0.97}Te$	8.5 $\pm$ 1.5	1.06918 $\mp$ 0.12
$V_{0.05}Sn_{0.95}Te$	7 $\pm$ 1.8	0.566037 $\mp$ 0.1
$V_{0.08}Sn_{0.92}Te$	6.8 $\pm$ 1.5	0.7547 $\mp$ 0.12

11508 | *Phys. Chem. Chem. Phys.*, 2025, **27**, 11499–11511

This journal is © the Owner Societies 2025

4. Conclusions

$V_x Sn_{1-x} Te$ NPs are synthesized by the chemical reflux method using glycine amino acid as a surfactant reactant and sodium borohydride as a reducing agent. The synthesized NPs are characterized by XRD, HRTEM, FEGSEM, XPS, Raman, and FTIR spectroscopy. HRTEM and FEGSEM showed that the average particle size of bare NPs is 5–50 nm, with different types of defect states. The charge transfer effects and the modification of the optical, magnetic, and magnetoconducting properties of NPs are experimentally validated by XPS, PL, magnetization, and magnetoconductance measurements, respectively. The DFT computations suggest that vanadium acts as a donor impurity, Sn vacancies make SnTe a p-type semiconductor, and SOC-induced spin canting and incorporating V bring magnetic ordering in bare and V-doped SnTe. The DC magnetization results showed a competing FM and AFM order due to the itinerant carrier-mediated RKKY interaction among interstitial and substitutional V ions and charge-transfer-induced BMPs. The linear variation of the $M–H$ curve at high field regimes is the signature of the superparamagnetic or paramagnetic surface contribution of the V-doped NPs. The intrinsic carrier localization in the BMP and reduction of hole concentration and surface degradation by substituting Sn vacancies with vanadium (V) atoms diminished the intrinsic carrier conductance and intensified the weak TSS conductance. The improved TSS conductance in the SnTe and V-doped compounds concurrently raises the WAL existing temperature, the fraction of an independent transport channel in the TSS, and the phase-coherent length. This indicates that the localization of intrinsic carriers (holes) by suitable charge transfer from the SnTe matrix and dopant (V) atoms to Sn vacancy positions and the minimizing hole concentration and surface degradation by substituting Sn vacancies are optimum strategies to suppress bulk transport and promote the TSS conductance in the TCI SnTe system. This anomalous behavior of magnetoresistance reveals magnetic anisotropy within the NPs. This proximity-coupled magnetic anisotropy makes V-doped SnTe a potential candidate for catalysis, thermoelectric, and spintronic applications.

Author contributions

Subhadip Ghosh: conceptualization, formal analysis, methodology, investigation, writing – original draft preparation and Sanjeev K. Srivastava: conceptualization, formal analysis, methodology, supervision, resources, writing – reviewing and editing.

Data availability

The data supporting this study are included in this article and as part of the ESI.†

Conflicts of interest

There are no conflicts to declare.

Acknowledgements

Notes and references

1 A. Phutela, P. Bhumla, M. Jain and S. Bhattacharya, *Sci. Rep.*, 2022, **12**, 21970.

2 C. Yan, F. Wei, Y. Bai, F. Wang, A. Zhang, S. Ma, W. Liu and Z. Zhang, *J. Mater. Sci. Technol.*, 2020, **44**, 223–228.

3 R. Mozumder, J. Wasmer, D. Antognini Silva, S. Blügel and P. Rüßmann, *Phys. Rev. Mater.*, 2024, **8**, 104201.

4 C.-W. Liu, Z. Wang, R. L. Qiu and X. P. Gao, *Nanotechnology*, 2020, **31**, 192001.

5 F. Le Mardelé, J. Wyzula, I. Mohelsky, S. Nasrallah, M. Loh, S. Ben David, O. Toledano, D. Tolj, M. Novak and G. Eguchi, *et al.*, *Phys. Rev. B*, 2023, **107**, L241101.

6 B. Lv, H. Weng, B. Fu, X. P. Wang, H. Miao, J. Ma, P. Richard, X. Huang, L. Zhao and G. Chen, *et al.*, *Phys. Rev. X*, 2015, **5**, 031013.

7 B.-Z. Tian, J. Chen, X.-P. Jiang, J. Tang, D.-L. Zhou, Q. Sun, L. Yang and Z.-G. Chen, *ACS Appl. Mater. Interfaces*, 2021, **13**, 50057–50064.

8 Z. Li, E. Xu, Y. Losovyj, N. Li, A. Chen, B. Swartzentruber, N. Sinitsyn, J. Yoo, Q. Jia and S. Zhang, *Nanoscale*, 2017, **9**, 13014–13024.

9 Q. Qu, B. Liu, H. Liu, J. Liang, J. Wang, D. Pan and I. K. Sou, *Nanoscale*, 2021, **13**, 18160–18172.

10 S. Bhattacharyya, G. Akhgar, M. Gebert, J. Karel, M. T. Edmonds and M. S. Fuhrer, *Adv. Mater.*, 2021, **33**, 2007795.

11 R. Vidal, H. Bentmann, J. Facio, T. Heider, P. Kagerer, C. Fornari, T. Peixoto, T. Figgemeier, S. Jung and C. Cacho, *et al.*, *Phys. Rev. Lett.*, 2021, **126**, 176403.

12 R. C. Vidal, A. Zeugner, J. I. Facio, R. Ray, M. H. Haghighi, A. U. Wolter, L. T. C. Bohorquez, F. Caglieris, S. Moser and T. Figgemeier, *et al.*, *Phys. Rev. X*, 2019, **9**, 041065.

13 Q. Liu, C.-X. Liu, C. Xu, X.-L. Qi and S.-C. Zhang, *Phys. Rev. Lett.*, 2009, **102**, 156603.

14 M. Li, C.-Z. Chang, L. Wu, J. Tao, W. Zhao, M. H. Chan, J. S. Moodera, J. Li and Y. Zhu, *Phys. Rev. Lett.*, 2015, **114**, 146802.

15 A. Alfonsov, K. Mehlawat, A. Zeugner, A. Isaeva, B. Büchner and V. Kataev, *Phys. Rev. B*, 2021, **104**, 195139.

This journal is © the Owner Societies 2025

Phys. Chem. Chem. Phys., 2025, **27**, 11499–11511 | **11509**

16 X. Kou, W. Jiang, M. Lang, F. Xiu, L. He, Y. Wang, X. Yu, A. Fedorov, P. Zhang and K. Wang, *J. Appl. Phys.*, 2012, **112**, 063912.

17 A. Grutter and Q. He, *Phys. Rev. Mater.*, 2021, **5**, 090301.

18 I. Costa, U. Mengui, E. Abramof, P. Rappl, D. Soares, S. de Castro and M. Peres, *Phys. Rev. B*, 2021, **104**, 125203.

19 Y. Choi, N. Jo, K. Lee, J. Yoon, C. You and M. Jung, *J. Appl. Phys.*, 2011, **109**, 07E312.

20 A. Gupta, A. Hillier, M. Telling and S. Srivastava, *Nanotechnology*, 2022, **33**, 215701.

21 J. Zhang, C.-Z. Chang, P. Tang, Z. Zhang, X. Feng, K. Li, L.-L. Wang, X. Chen, C. Liu and W. Duan, *et al.*, *Science*, 2013, **339**, 1582–1586.

22 D. Zhang, A. Richardella, D. W. Rench, S.-Y. Xu, A. Kandala, T. C. Flanagan, H. Beidenkopf, A. L. Yeats, B. B. Buckley and P. V. Klimov, *et al.*, *Phys. Rev. B: Condens. Matter Mater. Phys.*, 2012, **86**, 205127.

23 M. M. Otrokov, I. I. Klimovskikh, H. Bentmann, D. Estyunin, A. Zeugner, Z. S. Aliev, S. Gaß, A. Wolter, A. Koroleva and A. M. Shikin, *et al.*, *Nature*, 2019, **576**, 416–422.

24 A. M. Shikin, D. Estyunin, I. I. Klimovskikh, S. Filnov, E. Schwier, S. Kumar, K. Miyamoto, T. Okuda, A. Kimura and K. Kuroda, *et al.*, *Sci. Rep.*, 2020, **10**, 13226.

25 S. Harrison, L. J. Collins-McIntyre, P. Schönherr, A. Vailionis, V. Srot, P. A. van Aken, A. Kellock, A. Pushp, S. S. Parkin and J. Harris, *et al.*, *Sci. Rep.*, 2015, **5**, 15767.

26 T. Zhang, W. Pan, S. Ning, N. Qi, Z. Chen, X. Su and X. Tang, *Adv. Funct. Mater.*, 2023, **33**, 2213761.

27 N. Wang, D. West, J. Liu, J. Li, Q. Yan, B.-L. Gu, S. Zhang and W. Duan, *Phys. Rev. B: Condens. Matter Mater. Phys.*, 2014, **89**, 045142.

28 N. Mishra and G. Makov, *J. Alloys Compd.*, 2024, **986**, 174157.

29 S. Acharya, J. Pandey and A. Soni, *Appl. Phys. Lett.*, 2016, **109**, 133904.

30 S. Singh, H. Afzal, V. Kaushik, S. Kumar, P. Behera and R. Venkatesh, *Langmuir*, 2022, **38**, 3122–3128.

31 D. Feng, Z.-H. Ge, Y.-X. Chen, J. Li and J. He, *Nanotechnology*, 2017, **28**, 455707.

32 J. S. Dyck, P. Hájek, P. Lošťák and C. Uher, *Phys. Rev. B: Condens. Matter Mater. Phys.*, 2002, **65**, 115212.

33 J. Dyck, Č. Drašar, P. Lošťák and C. Uher, *Phys. Rev. B: Condens. Matter Mater. Phys.*, 2005, **71**, 115214.

34 A. Alfonsov, J. Facio, K. Mehlawat, A. Moghaddam, R. Ray, A. Zeugner, M. Richter, J. van den Brink, A. Isaeva and B. Büchner, *et al.*, *Phys. Rev. B*, 2021, **103**, L180403.

35 A. Alfonsov, K. Mehlawat, A. Zeugner, A. Isaeva, B. Büchner and V. Kataev, *Phys. Rev. B*, 2021, **104**, 195139.

36 A. Kaminski and S. D. Sarma, *Phys. Rev. Lett.*, 2002, **88**, 247202.

37 S. D. Sarma, E. Hwang and A. Kaminski, *Phys. Rev. B: Condens. Matter Mater. Phys.*, 2003, **67**, 155201.

38 P. Wolff, R. Bhatt and A. Durst, *J. Appl. Phys.*, 1996, **79**, 5196–5198.

39 M. Heming and G. Lehmann, *Z. Naturforsch., A*, 1983, **38**, 149–153.

40 D. Vaknin, D. Davidov, V. Zevin and H. Selig, *Phys. Rev. B: Condens. Matter Mater. Phys.*, 1987, **35**, 6423–6431.

41 J. König, H.-H. Lin and A. H. MacDonald, *Phys. Rev. Lett.*, 2000, **84**, 5628.

42 M. Berciu and R. Bhatt, *Phys. Rev. Lett.*, 2001, **87**, 107203.

43 J.-J. Zhu, D.-X. Yao, S.-C. Zhang and K. Chang, *Phys. Rev. Lett.*, 2011, **106**, 097201.

44 G. C. Papaefthymiou, *Nano Today*, 2009, **4**, 438–447.

45 A. Wolos, A. Drabinska, J. Borysiuk, K. Sobczak, M. Kaminska, A. Hruban, S. G. Strzelecka, A. Materna, M. Piersa and M. Romaniec, *et al.*, *J. Magn. Magn. Mater.*, 2016, **419**, 301–308.

46 A. Wolos, S. Szyszko, A. Drabinska, M. Kaminska, S. Strzelecka, A. Hruban, A. Materna and M. Piersa, *Phys. Rev. Lett.*, 2012, **109**, 247604.

47 H. Steinberg, J.-B. Laloë, V. Fatemi, J. S. Moodera and P. Jarillo-Herrero, *Phys. Rev. B: Condens. Matter Mater. Phys.*, 2011, **84**, 233101.

48 A. Drabińska, M. Kamińska, A. Wołoś, W. Strupinski, A. Wysmołek, W. Bardyszewski, R. Bożek and J. M. Baranowski, *Phys. Rev. B: Condens. Matter Mater. Phys.*, 2013, **88**, 165413.

49 V. L. Nguyen, D. C. Nguyen, H. Hirata, M. Ohtaki, T. Hayakawa and M. Nogami, *Adv. Nat. Sci.: Nanosci. Nanotechnol.*, 2010, **1**, 035012.

50 S. K. Cgandomani, B. Khoshnevisan and R. Yousefi, *J. Lumin.*, 2018, **203**, 481–485.

51 R. Walstedt and A. Narath, *Phys. Rev. B*, 1972, **6**, 4118.

52 H.-T. He, G. Wang, T. Zhang, I.-K. Sou, G. K. Wong, J.-N. Wang, H.-Z. Lu, S.-Q. Shen and F.-C. Zhang, *Phys. Rev. Lett.*, 2011, **106**, 166805.

53 A. Wolos and A. Drabinska, *J. Cryst. Grow.*, 2014, **401**, 314–318.

54 M. Sharma, D. Mishra and J. Kumar, *Phys. Rev. B*, 2019, **100**, 045151.

55 P. Giannozzi, S. Baroni, N. Bonini, M. Calandra, R. Car, C. Cavazzoni, D. Ceresoli, G. L. Chiarotti, M. Cococcioni and I. Dabo, *et al.*, *J. Phys.: Condens. Matter*, 2009, **21**, 395502.

56 Y. Xie, Q. He, J. Guo, X. Li, J. Wei, Y. Zhang, C. Gu, P. Lu and X. Shen, *Adv. Opt. Mater.*, 2024, **12**, 2400632.

57 Y. Su, C. Ding, Y. Yao, R. Fu, M. Xue, X. Liu, J. Lin, F. Wang, X. Zhan and Z. Wang, *Nanotechnology*, 2023, **34**, 505206.

58 D. Hull and D. J. Bacon, *Introduction to dislocations*, Elsevier, 2011, vol. 37.

59 V. Varadaraajan, PhD thesis, The University of Michigan, 2015.

60 S. Ahmad, A. Singh, S. Bhattacharya, M. Navaneethan, R. Basu, R. Bhatt, P. Sarkar, K. Meshram, A. Debnath and K. Muthe, *et al.*, *ACS Appl. Energy Mater.*, 2020, **3**, 8882–8891.

61 H.-S. Yoon, J. Lee, J. Park, J.-W. Oh and Y.-C. Kang, *Phys. Status Solidi A*, 2022, **219**, 2200059.

62 M. A. Stranick and A. Moskwa, *Surf. Sci. Spectra*, 1993, **2**, 50–54.

63 A. Saini, K. Dhanwant, K. Dewangan, R. Thirumoorthi, A. Jaiswal, I. Bahadur, F. Mohammad and A. A. Soleiman, *Results Mater.*, 2023, **18**, 100397.

11510 | *Phys. Chem. Chem. Phys.*, 2025, **27**, 11499–11511

This journal is © the Owner Societies 2025

64 R. Zimmermann, R. Claessen, F. Reinert, P. Steiner and S. Hüfner, *J. Phys.: Condens. Matter*, 1998, **10**, 5697.

65 S. Sugai, K. Murase and H. Kawamura, *Solid State Commun.*, 1977, **23**, 127–129.

66 S. Khosravi Ghandomani, B. Khoshnevisan and R. Yousefi, *J. Mater. Sci.: Mater. Electron.*, 2018, **29**, 18989–18996.

67 P. Makuła, M. Pacia and W. Macyk, *How to correctly determine the band gap energy of modified semiconductor photocatalysts based on UV-Vis spectra*, 2018.

68 D. Mosca, J. Varalda and C. Dartora, *Phys. Rev. B*, 2023, **108**, 134410.

69 M. Schlaak and A. Weiss, *Z. Naturforsch., A*, 1972, **27**, 1624–1633.

70 V. Fernandes, R. Mossanek, P. Schio, J. Klein, A. De Oliveira, W. Ortiz, N. Mattoso, J. Varalda, W. Schreiner and M. Abbate, *et al.*, *Phys. Rev. B: Condens. Matter Mater. Phys.*, 2009, **80**, 035202.

71 Z. Ma, C. Wang, Y. Chen, L. Li, S. Li, J. Wang and H. Zhao, *Mater. Today Phys.*, 2021, **17**, 100350.

72 C. Ko, Z. Yang and S. Ramanathan, *ACS Appl. Mater. Interfaces*, 2011, **3**, 3396–3401.

73 D. I. Khomskii, *Transition metal compounds*, Cambridge University Press, 2014.

74 J. Vithayathil, D. MacLaughlin, E. Koster, D. L. Williams and E. Bucher, *Phys. Rev. B: Condens. Matter Mater. Phys.*, 1991, **44**, 4705.

75 J. Kreissl, W. Gehlhoff, P. Omling and P. Emanuelsson, *Phys. Rev. B: Condens. Matter Mater. Phys.*, 1990, **42**, 1731.

76 V. Ivanshin, V. Yushankhai, J. Sichelschmidt, D. Zakharov, E. Kaul and C. Geibel, *Phys. Rev. B: Condens. Matter Mater. Phys.*, 2003, **68**, 064404.

77 A. Nakajima, *Talanta*, 2002, **57**, 537–544.

78 A. Nakajima, *Talanta*, 2002, **57**, 537–544.

79 H.-Z. Lu, J. Shi and S.-Q. Shen, *Phys. Rev. Lett.*, 2011, **107**, 076801.

80 N. Berchenko, R. Vitchev, M. Trzyna, R. Wojnarowska-Nowak, A. Szczerbakow, A. Badyla, J. Cebulski and T. Story, *Appl. Surf. Sci.*, 2018, **452**, 134–140.

81 P. Ngabonziza, R. Heimbuch, N. De Jong, R. Klaassen, M. Stehno, M. Snelder, A. Solmaz, S. Ramankutty, E. Frantzeskakis and E. Van Heumen, *et al.*, *Phys. Rev. B: Condens. Matter Mater. Phys.*, 2015, **92**, 035405.